frontiers | Frontiers in Marine Science

TYPE Original Research
PUBLISHED 24 March 2025
DOI 10.3389/fmars.2025.1556924

OPEN ACCESS

EDITED BY
Giovanni Bracco,
Polytechnic University of Turin, Italy

REVIEWED BY
Carlos Pérez-Collazo,
University of Vigo, Spain
Peng Chen,
Shanghai Jiao Tong University, China
Dan Hu,
Wuhan University of Technology, China

*CORRESPONDENCE
Chuanli Xu
xuchuanli@stu.ouc.edu.cn

RECEIVED 07 January 2025
ACCEPTED 03 March 2025
PUBLISHED 24 March 2025

CITATION
Chen X, Yu X, Dong X, Xu C, Liu Z and Wang L (2025) Sediment scouring at the foundation of a coupled wind and wave device: a numerical study.
Front. Mar. Sci. 12:1556924.
doi: 10.3389/fmars.2025.1556924

Sediment scouring at the foundation of a coupled wind and wave device: a numerical study

Xin Chen[1], Xiang Yu[1], Xiaochen Dong[2], Chuanli Xu[2]*, Zhen Liu[2] and Lihui Wang[2]

[1]Huadian (Fujian) Wind Power Co., Ltd., Fuzhou, China, [2]Shandong Provincial Key Laboratory of Ocean Engineering, Ocean University of China, Qingdao, China

Introduction: Developing wind-wave coupled devices is becoming a research hotspot in offshore renewable energy. While previous studies have primarily concentrated on the hydrodynamic performance of such devices, few have addressed sediment scouring near the foundation, which is critical to their safety.

Methods: Therefore, based on the design of a wind-wave coupled device integrating an offshore fixed wind turbine, a sediment scouring model is developed using the commercial computational fluid dynamics platform Flow-3D®. The numerical model is validated using experimental test data, and the sediment scouring and deposition under the combined effects of waves and currents are investigated.

Results: The results indicate that the oscillating water column tube array can expand the scouring area but have a minor influence on the maximum scouring depth. In addition, due to the sheltered effect of the oscillating water column tubes, the maximum scouring depth near the piles at the far end can be reduced.

Discussion: By optimizing the distance between the tube ends and the seabed, the maximum scouring depth can be reduced by 22.8%, which is beneficial to the safety and stability of the foundation of the coupled device. The key findings of this study provide a more comprehensive design basis for the development and engineering practice of the wind-wave coupled device.

KEYWORDS

offshore wind turbine, wave energy, oscillating water column, coupled device, sediment scouring, numerical simulation

1 Introduction

Green and sustainable development has become an irresistible trend globally, and most countries have agreed to develop renewable energy (Yang et al., 2019). There are abundant renewable energies in the ocean, such as wind, wave, and tidal streams, with large reserves and high quality to become a critical part of the future energy mix (Rehman et al., 2023). Of

all the ocean renewable energies, offshore wind energy technology is the most mature and widely used one, and it has entered the industrialization stage. Unlike onshore wind energy, offshore wind has advantages, including higher power flux density, low turbulence intensity, small wind shears, and small covering areas (De Azevedo et al., 2016). In addition, wave energy is a promising ocean renewable energy, having the advantage of high power flux density, wide distribution, high accessibility, and low environmental impacts.

Wave energy converting technologies have yet to converge compared to offshore wind energy. The construction cost and the levelized cost of energy (LCOE) are still high, which restricts the commercial development of wave energy. On the other hand, according to the associated relationship between the wind and wave energies, the areas with excellent wind power resources have good wave power reserves. Consequently, the integrated development of the wind and wave energies to share the foundation and electrical system is an alternative solution to reduce the construction cost of the wave energy device significantly. Furthermore, the coupled wave-wind energy device not only enhances the utilization rate of the ocean space but obtains higher power production density and reduces the LCOE of the device, promoting the industrialization process of the ocean renewable energies (Wan et al., 2024). The offshore wind turbines are mainly the fixed type, including the mono-pile, jacket platform, and high-rise platform pile foundation. The sediment scouring of the foundation should be considered to ensure the safety and stability of the entire structure.

The studies on the sediment scouring problem of the foundation started early from the mono-pile. Olsen and Kjellesvig (1998) investigated the local scouring near a vertical cylinder using the three-dimensional (3D) numerical simulation and proposed a fully coupled flow-scour model to predict the equilibrium scour depth. Roulund et al. (2005) calculated the scour of non-cohesive sediment near a vertical pile using the 3D k-Ω turbulence model and reported that the bed shear stress decreased significantly at the equilibrium state compared to the initial stage. Zhao et al. (2010) predicted the scouring process around a cylinder using the k-Ω turbulence model and found that the shedding number of the horseshoe vortex decreased as the cylinder height decreased. Bordbar et al. (2021) compared the scouring performance of the square pier and diamond pier and reported that the increasing speed of the scouring depth for the square pier was larger, and the equilibrium scouring pit was deeper. Dixen et al. (2013) studied the scouring process around a semi-buried sphere and found that the scouring depth and velocity increased as the horseshoe vortex and lee-wake flows were considered. Yu et al. (2016) investigated the geometrical shape of the equilibrium scouring pit of a bucket foundation in one-way and two-way water flows and reported that the equilibrium scouring depth (ESD) in the two-way flow was 16% less than that in the one-way flow. Yu et al. (2019) analyzed the scouring process of the bucket foundation under the integrated actions of the wave and tidal stream and found that the scouring area under the integrated actions was larger than that only in the tidal current.

For the multiple-pile structures, Liu et al. (2022) investigated the scouring mechanism of the two vertical piles with different gap ratios and deployment configurations. For the tandem configuration, the ESD increased first and then converged as the gap increased. The ESD was identical to the single pile for the side-by-side configuration, as the gap ratio was larger than 0.5. The ESD maintained approximately unchanged for the staggered configuration as the gap increased. Amini et al. (2012) conducted an experimental study on a pile group and found that the shielding and jetting effects caused the local flow and scouring near the piles to be more complicated. Liang et al. (2017) confirmed the viewpoint and proposed that the shield and jetting effects reduced as the gaps between the piles increased. Li et al. (2022) investigated the scouring problems of a multi-bucket jacket foundation of the wind turbine and reported that an increase in the scouring depth could cause a decrease in the horizontal bearing capacity of the foundation, and the scouring area had minor effects on the bearing capacity. Hu et al. (2021) experimentally studied the scouring evolution and pattern of a tripod foundation under the joint actions of the waves and currents in a wave flume and reported that higher Froude and Euler numbers could enhance the integration of waves and currents, resulting in a larger ESD. Welzel et al. (2019) evaluated the scouring development process of a jacket structure under the coupled actions of the waves and currents and reported the ESDs in the upstream and downstream were relatively larger and smaller, respectively. Kim et al. (2014) conducted a numerical simulation on the scour around the tandem and side-by-side piles under the clear water condition, and the numerical predictions agreed well with the on-site measured data (Liu et al., 2008). The maximum scouring depth for the side-by-side configuration increased as the distance between the piles decreased, which increased first and then decreased for the tandem configuration. Zhang et al. (2017) investigated the local scouring mechanism around three piles with various configurations under a constant flow condition using the numerical method and reported that the scour pit shapes and depths for different configurations were different.

The existing studies have conducted abundant investigations on the scour of the fixed offshore wind turbine foundation. Evaluating the scour at the foundations has become a critical task during the design of the offshore wind turbine. For the coupled wind and wave devices, the existing studies mainly focused on the hydrodynamic characteristics and energy-harvesting performance (Wan et al., 2024). The scour is a crucial factor in causing the instability of the wind turbine foundation (Zhang et al., 2022, Zhang et al., 2023), and there was a case that the scour problem caused the decommission of the wind turbine (Menéndez-Vicente et al., 2023). It has been proved that the integrated actions of the waves and currents could significantly enhance the scouring area and depth around the foundation of the offshore wind turbine (Qi and Gao, 2014). The existence of the wave energy converter (WEC) can affect the foundation forces, structural stability, scouring area, and, subsequently, the safety of the coupled device.

From the literature review, there are few specific studies on the scour problems associated with the coupled wind and wave device. There remains a gap in research regarding the design of the WEC and its effects on sediment scouring and deposition around the foundation. Moreover, the coupled wind and wave device creates a

more complex hydrodynamic environment due to the interactions among waves, currents and solid structures. In this study, a coupled device consisting of a wind turbine and an oscillating water column (OWC) WEC installed on a high-rise platform pile foundation is proposed. A numerical model to evaluate the scour around the foundation is set up based on the commercial computational fluid dynamics (CFD) platform FLOW-3D®. The effects of the wind-wave coupled device on the scour near the foundation are predicted and analyzed. The main contribution of this study is to clarify the effect of the added WEC on the scouring conditions around the wind turbine foundation, in order to assess whether the coupled device affects the safety of the existing foundation. The results provide valuable insights for the design and engineering applications of the coupled wind and wave device.

The rest of this paper is organized as follows: The foundations of the numerical model are described in Section 2. Model setup and validations are presented in Section 3. In Section 4, the sediment scouring performance of two types of devices is compared. Conclusions can be found in Section 5.

2 Governing equations in the numerical model

The numerical model is established based on the commercial CFD platform FLOW-3D®, and the governing equations in the hydrodynamic model are the continuity equation and the Naiver-Stokes equation (Flow Science, 2016). The continuity equation (Equation 1) can be expressed as follows:

$$\frac{V_F\partial\rho}{\partial t}+\frac{\partial}{\partial x}(\rho u A_x)+\frac{\partial}{\partial y}(\rho v A_y)+\frac{\partial}{\partial z}(\rho w A_z)=R_{DIF} \tag{1}$$

where V_F is the volume fraction of the flow section; ρ and t represent the water density and time; u, v, and w are the velocity components in the x, y, and z directions, respectively; A_x, A_y, and A_z are the area fractions of the flowing fluid in the x, y, and z directions, respectively; R_{DIF} is the turbulent diffusion term, which can be written as Equation 2:

$$R_{DIF}=\frac{\partial}{\partial x}\left(\nu_\rho A_x\frac{\partial\rho}{\partial x}\right)+\frac{\partial}{\partial y}\left(\nu_\rho A_y\frac{\partial\rho}{\partial y}\right)+\frac{\partial}{\partial z}\left(\nu_\rho A_z\frac{\partial\rho}{\partial z}\right) \tag{2}$$

where $\nu_\rho = S_c\mu/\rho$ and μ is the coefficient of momentum diffusion; S_c is the reciprocal of the turbulent Schmidt number, and the value is set as 0.7 (Wang et al., 2020).

The Naiver-Stokes equations (Equations 3–5) for the velocity components u, v, and w are defined as follows:

$$\frac{\partial u}{\partial t}+\frac{1}{V_F}\left(uA_x\frac{\partial u}{\partial x}+vA_x\frac{\partial u}{\partial y}+wA_z\frac{\partial u}{\partial z}\right)=-\frac{1}{\rho}\frac{\partial p}{\partial x}+G_x+f_x \tag{3}$$

$$\frac{\partial v}{\partial t}+\frac{1}{V_F}\left(uA_x\frac{\partial v}{\partial x}+vA_y\frac{\partial v}{\partial y}+wA_z\frac{\partial v}{\partial z}\right)=-\frac{1}{\rho}\frac{\partial p}{\partial y}+G_y+f_y \tag{4}$$

$$\frac{\partial w}{\partial t}+\frac{1}{V_F}\left(uA_x\frac{\partial w}{\partial x}+vA_y\frac{\partial w}{\partial y}+wA_z\frac{\partial w}{\partial z}\right)=-\frac{1}{\rho}\frac{\partial p}{\partial z}+G_z+f_z \tag{5}$$

where G_x, G_y, and G_z are the components of the gravitational acceleration in the x, y, and z directions, respectively; f_x, f_y, and f_z are the components of the viscous acceleration in the x, y, and z directions, respectively; p is the pressure of water.

The bed load discharge $q_{b,i}$ can be defined as Equation 6:

$$q_{b,i}=\Phi_i\left[g\left(\frac{\rho_i-\rho}{\rho}d_i^3\right)\right]^{1/2} \tag{6}$$

where g, ρ_i, and d_i represent the gravitational acceleration, sediment density, and sediment median diameter, respectively; Φ_i is the coefficient of the bed load discharge, which is determined by the local Shields number (Equation 7):

$$\Phi_i=\beta(\theta_i-\theta_{cr})^{1.5} \tag{7}$$

where β is the bed load coefficient, which is set at 8.0 according to the experiences and relative reference (Fernandez Luque and Van Beek, 1976); θ_{cr} is the threshold Shields number; θ_i is the local Shields number, which is defined according to the local bed shear stress τ (Equation 8):

$$\theta_i=\frac{\tau}{\|g\|d_i(\rho_i-\rho)} \tag{8}$$

The governing equation (Equation 9) of the suspended load is the convection-diffusion equation:

$$\frac{\partial \mathbf{C_{s,i}}}{\partial \mathbf{t}}+\nabla\cdot(\mathbf{u_{s,i}C_{s,i}})=\nabla\cdot\nabla(\mathbf{DC_{s,i}}) \tag{9}$$

where $C_{s,i}$ is the mass concentration of the suspended sediment; D is the sediment diffusion coefficient; $u_{s,i}$ is the velocity of the suspended load.

In addition, the entrainment lift velocity of the sediment u_{lift} can be defined as Equations 10, 11:

$$u_{lift}=\alpha N_s d_*^{0.3}(\theta_i-\theta_{cr})^{1.5}\sqrt{\frac{(\rho_i-\rho)d_i\|g\|}{\rho}} \tag{10}$$

$$d_*=d_i\left[\frac{\rho(\rho_i-\rho)\|g\|}{\mu_f^2}\right]^{\frac{1}{3}} \tag{11}$$

where α is the entrainment parameter, with a value of 0.018 (Mastbergen and Van Den Berg, 2003); N_s is the outward pointing normal to the packed bed interface; u_f represents the dynamic viscosity of water.

Furthermore, the settling velocity of the sediment $u_{settling}$ can be expressed as Equation 12:

$$u_{\mathbf{settling}}=\frac{\nu_f}{d_i}\left[(10.36^2+1.049d_*^3)^{0.5}-10.36\right] \tag{12}$$

where ν_f is the kinematic viscosity of water.

3 Setup and validations of the numerical model

3.1 Numerical model setup

The numerical model is established based on a research project to validate the integration feasibility of a fixed wind turbine and a multi-tube OWC-WEC, as shown in Figure 1. The wind turbines are installed in an offshore wind farm in Haitan Strait operated by China Huadian Corporation Ltd. in Fujian Province, China. The main parameters of the device are listed in Table 1. The foundation of the wind turbine is a high-rise pile cap, and eight inclined piles have a slope ratio of 5:1. The OWC-WEC is fixed on the side wall of the reinforced concrete cap with six tubes in a 2×3 configuration and a shared chamber. The OWC-WEC is installed facing the predominant wave direction to improve its efficiency in harnessing wave energy. A horizontal duct is connected to the shared chamber to install a self-rectifying air turbine and an electric generator for power output. The electricity is transmitted to the electrical devices of the wind turbine for integration. The OWC-WEC and wind turbine will be tested for at least one year to validate their joint operation feasibility. The multiple tubes are easy to manufacture for modularization. The sea trials of the OWC-WEC installed on the foundation of an offshore wind turbine can provide sufficient *in-situ* operation data for the OWC-WEC and the wind turbine, including the hydrodynamic and pneumatic characteristics and electrical performances, which is valuable for further deployment of multi-tubes with large-scale wave power conversion.

The numerical model of the foundation scouring for a coupled wave-wind device is set up using the commercial CFD platform Flow-3D® 11.2 (Flow Science, 2016). The governing equations of the numerical model are the continuity equation and the Reynolds-averaged Naiver-Stokes equations. A cubic computational domain is established for numerical simulations. Since the wind turbine with the reinforced concrete cap and the shared chamber and duct used to install the air turbine do not interact with the water flow, these components are excluded in the numerical model, as they are considered to have no impact on sediment scouring and seabed transportation near the foundation. Eight high-rise piles are deployed, as the actual engineering, with a pile diameter of d_z =

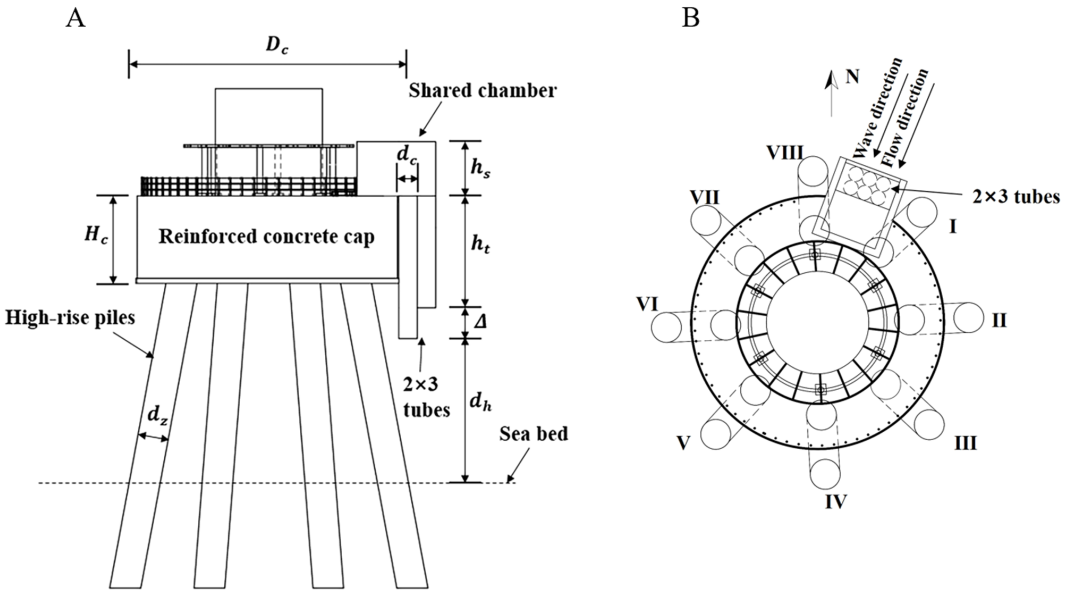

FIGURE 1
A coupled wind-wave device integrating an OWC-WEC and an offshore wind turbine. **(A)** Side view; **(B)** Top view.

TABLE 1 Main parameters of the coupled wind-wave device.

Parameter	Symbol	Value	Parameter	Symbol	Value
Height of the reinforced concrete cap	H_c	5.6 m	Difference of the short and long tubes	Δ	2.0 m
Height of the shared chamber	h_s	3.5 m	Diameter of the tubes	d_c	0.8 m
Height of the short tubes	h_t	7.0 m; 9.5 m; 12.0 m; 14.5 m	Distance between the seabed and the longest tube	d_h	2.5 m; 5.0 m; 7.5 m; 10.0 m
Diameter of the reinforced concrete cap	D_c	17.5 m	Diameter of the high-rise piles	d_z	2.0 m

2.0 m. The length, width, and height of the computational domain are 45.0 dz, 20.0 dz, and 10.0 dz, respectively. As for the turbulence model, the RNG k-ε model has been proven to be suitable for addressing sediment scouring issues (Analytis, 2003; Okhravi et al., 2023; Zheng et al., 2024). Therefore, the RNG k-ε turbulence model is employed to close the equations and handle the turbulences near the walls in the present model. The finite volume method is used to discretize the governing equations. The generalized minimal residual method (Steven et al., 1990) with implicit schemes is employed for the pressure-velocity coupling solution. The mesh structures of the coupled model are depicted in Figure 2. Regular hexahedral meshes with a characteristic length of 1.5 dz are used in the numerical model. The meshes near the tubes, piles, and seabed are refined, with a characteristic length of 0.1 dz. The total number of meshes is approximately 3.0 million.

In the computational domain, the left and right boundaries are set as the flow inlet and outflow boundary conditions, respectively. The top and bottom boundaries are set as the pressure outlet and wall boundary conditions. Two side walls are set as the symmetry boundary condition. All environmental parameters refer to the local oceanic conditions in Fujian, China. In the sediment scouring model, the critical Shields number is fixed at 0.05. The incident waves employ a regular wave scenario with a wave height of 1.0 m and a wave period of 5.0 s. The current velocity is fixed at 1.0 m/s. The median sediment diameter is 0.15 mm, and the angle of repose is 32°.

3.2 Numerical model validation

The numerical model is validated by comparing the predictions and experimental results from a previous study (Yeh et al., 2009), which is expected to prove the predicting capability of the interactions between the water and sediment. In the experimental test, the sand bed was paved in a flume to be impacted by an underwater jet flow. The evolution of the scouring pit was observed for a test duration of 20.0 min. An acoustic Doppler velocimetry was used to measure and record the scouring depth at a position near the jet center to avoid affecting the jet flow. The diameter of the jet nozzle was 0.127 m, and the jet flow velocity was 2.05 m/s. The jet height and water depth were 0.76 m and 1.83 m, respectively. The median sediment diameter was 0.258 mm, and the grain density was 2.65×10^3 kg/m^3.

The comparison of the scour depth variation at different time points at the measuring point in the scouring pit between numerical and experimental results is depicted in Figure 3. The numerical predictions are derived at the jet center, which is slightly different from the experimental setup. At the initial point for t = 3.0 min, the scour depth difference between experimental and numerical results is larger, by approximately 10.1%, which could be caused by the instability of the initial pit. The difference between the numerical and experimental results decreases as the time increases, and the difference at t = 20.0 min decreases to 6.0%. The average difference is approximately 7.1%.

The numerical prediction and experimental result of the final cross-section profile of the scouring pit are compared in Figure 4. Generally, the numerical and experimental final profiles of the scouring pit agree well. The final maximum scouring depth difference between numerical and experimental results is approximately 6.0%. The overall profile difference might be caused by the difference in the measuring point. The angle of the pit slope has a difference of 8.0% in numerical and experimental results. The angle of repose in the numerical model is set at 45°, which was not provided in the experimental report and might cause the numerical error. The comparison results indicate that the numerical model shows its capability to predict sediment scouring for further studies.

4 Results and discussions

4.1 Problem description

The computational domain of the numerical model for the sediment scouring at the foundation of the coupled wind-wave

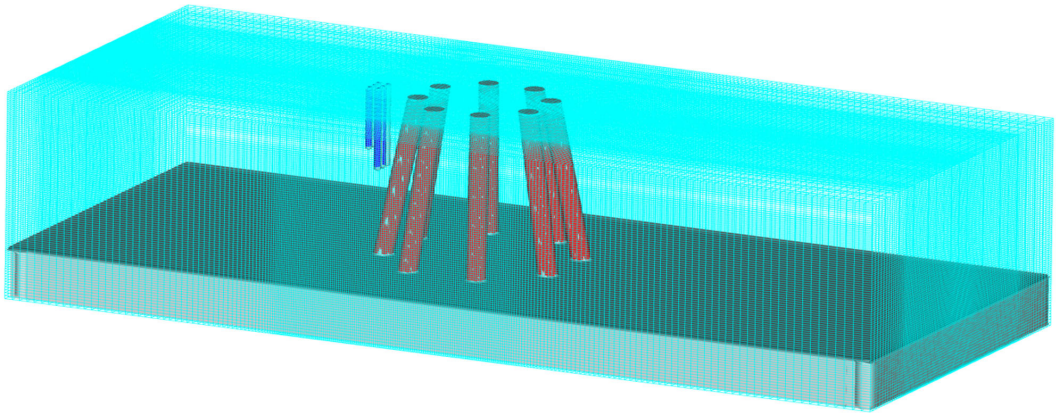

FIGURE 2
Mesh structures of the model.

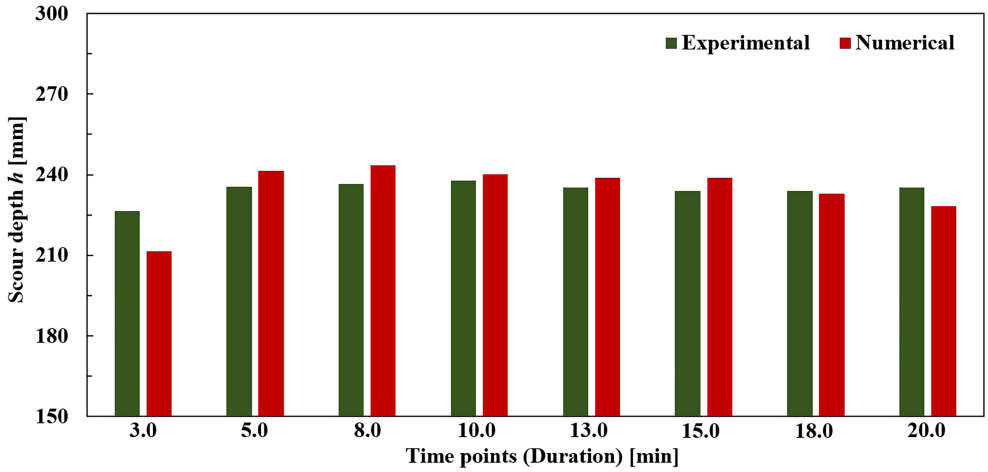

FIGURE 3
Comparison of the depth variation at the measuring point in the validation case.

device is depicted in Figure 5. The center of the pile group is located at X = 20.0 dz and Y = 10.0 dz. Six tubes are arranged in two rows and three columns at X = 15.0 dz and Y = 10.0 dz. The tube diameter is d_c = 0.8 m. The height difference between two rows of tubes is 1.0 dz, and longer tubes are close to the piles. The computational domain is divided into three parts: water, air, and sediment sub-domains. The sediment, water, and air sub-domains have the heights of 2.5 dz, 6.0 dz, and 1.5 dz, respectively. The distance between the seabed and the longest tube is defined as d_h, varying from 1.25 dz to 2.50 dz, 3.75 dz, and 5.00 dz. Eight piles are numbered from I to VIII in a clockwise order. The incident wave and current directions are defined as positive along the X-direction.

4.2 Sediment scouring near the piles of the original wind turbine

First, the sediment scouring near the piles of the original wind turbine under the joint actions of incident waves and currents is simulated for comparison. During the trial simulations, it was found

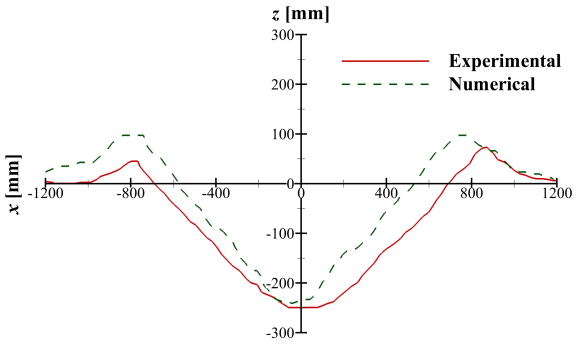

FIGURE 4
Comparison of the cross-section profile of the scouring pit in the validation case.

that sediment scouring and deposition begin to converge after 30.0 min in this study. Therefore, the simulation time is fixed at 30.0 min, and the time points at 5.0 min, 10.0 min, 20.0 min, and 30.0 min are selected as the typical representing time points for analysis of all results.

The water flow velocity near the seabed is a critical parameter affecting sediment incipient motion and its scouring and deposition. Therefore, the velocity contours of the water flow right above the seabed on the X-Y plane (Z = 0) at four typical time points are depicted in Figure 6. The distribution characteristics of the water flow velocities above the seabed for four typical time points have no significant difference, indicating that the incident waves have minor influences on the flow field near the seabed. In addition, the distribution of the water flow velocity in the X-Y plane is symmetrical to the Y = 10.0 dz axis. The velocities at two sides of the piles are accelerated with larger values, which are more significant for piles I, II, VII, and VIII. At the positions in front of and in the rear of the piles, the water flow velocities are relatively lower. Piles III and VI are in the wake of piles II and VII, respectively, and the velocities near the piles are significantly affected by the wake flow. Furthermore, the lowest velocities can be found in the wake of piles IV and V. A similar phenomenon has also been observed in studies on the coupled group pile foundations (Liu et al., 2022).

As the flow field is symmetrical to the axis of Y = 10.0 dz in the computational domain, the velocity contours of the water flow on the X-Z planes are only shown in half of the domain in Figure 7. Two typical X-Z planes are employed: Y = 11.75 dz including the piles I and IV and Y = 14.50 dz including piles II and III. The velocity contours can clearly show the influences of incident waves on the flow field. As the distance between piles I and IV is large, as shown in Figure 7A, the flow field between two piles is affected less by the front one, resulting in more turbulences and larger velocity values above the seabed between piles I and IV. For piles II and III, as shown in Figure 7B, the distance is relatively small, and a low-velocity zone can be observed between the piles with a limited area.

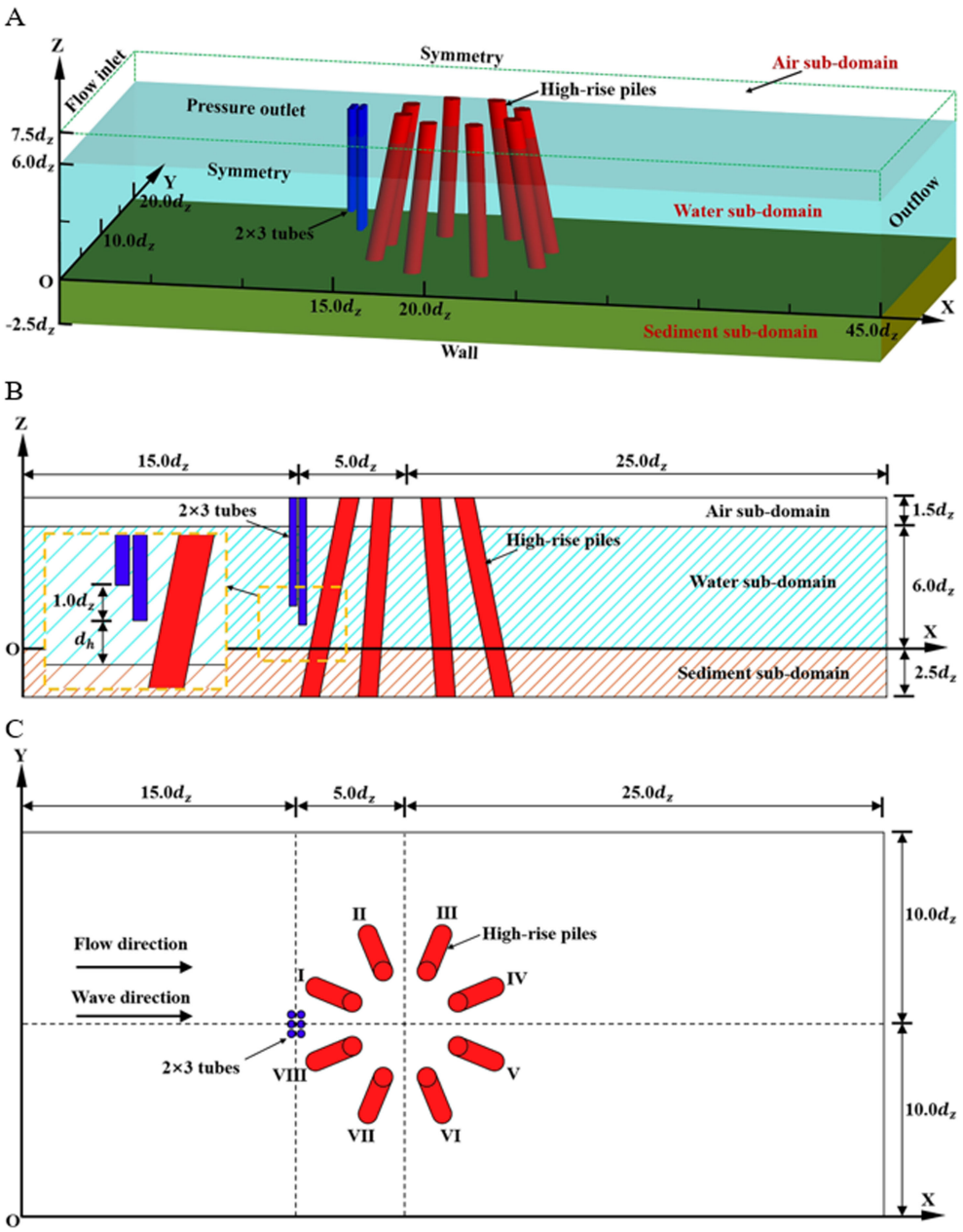

FIGURE 5
Computational domain of the numerical model. **(A)** 3D bird view; **(B)** Side view; **(C)** Top view.

The development of sediment scouring and deposition near the piles in the initial 30.0 min can be reflected by the depth variation contours in Figure 8. The basic distribution characteristics at four typical time points are similar, with different scouring and deposition values. The sediment scouring and deposition are also symmetric to the $Y = 10.0$ dz axis. The sediment scouring can be observed at two sides of the piles because of incident water flow velocity enhancement. On the other hand, the sediment depositions are found in the front and back of the piles, where the water flow velocities are observed to be reduced, especially for piles III and VI, which have the most deposition depths.

The seabed depth variations in the 30.0 min calculation duration at four points which are near four piles I to IV in a half side with the largest scouring depth are depicted in Figure 9. The coordinate (in the *X*-*Y* plane) details of the monitoring points are listed as the follows: (15.5 dz, 11.5 dz) for Pile I; (18.1 dz, 13.8 dz) for Pile II; (21.8 dz, 13.9 dz) for Pile III; (24.5 dz, 11.6 dz) for Pile IV. It can be observed that the scouring depths for Pile III are significantly smaller than the points for other piles during the calculation period. From the velocity analysis in the contour figures, it could be concluded that Pile III is sheltered by Pile II and the velocities at two sides of the pile reduce gradually, resulting in a reduction in the sediment carrying capability of the water flow and a settlement of the suspended load near the pile. On the other hand, the distance between piles I and IV is relatively larger, and the sheltered effects of Pile I to the Pile IV are relatively

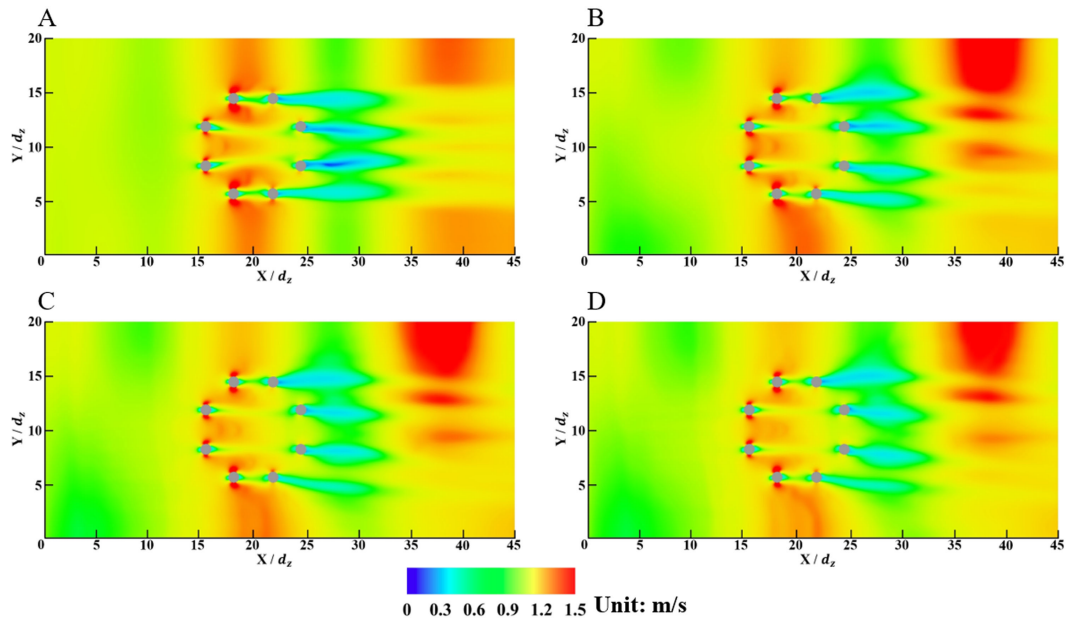

FIGURE 6
Velocity contours of the water flow on an *X*-*Y* plane for the original wind turbine (*Z* = 0). **(A)** *t* = 5.0 min; **(B)** *t* = 10.0 min; **(C)** *t* = 20.0 min; **(D)** *t* = 30.0 min.

weak, resulting in more scouring near Pile IV than that near Pile III. For piles arranged in a front-back configuration, the scour depth increases with the distance between the piles, which aligns with the findings of this study (Liu et al., 2022). The converged scouring depth for the four points are 0.42 dz, 0.51 dz, 0.32 dz, and 0.52 dz, respectively.

4.3 Sediment scouring near the piles of the wind-wave coupled device

The velocity contours of the water flow near the piles of the wind-wave coupled device on an *X*-*Y* plane (*Z* = 0) at *t* = 30.0 min for various values of d_h are depicted in Figure 10. The overall effects

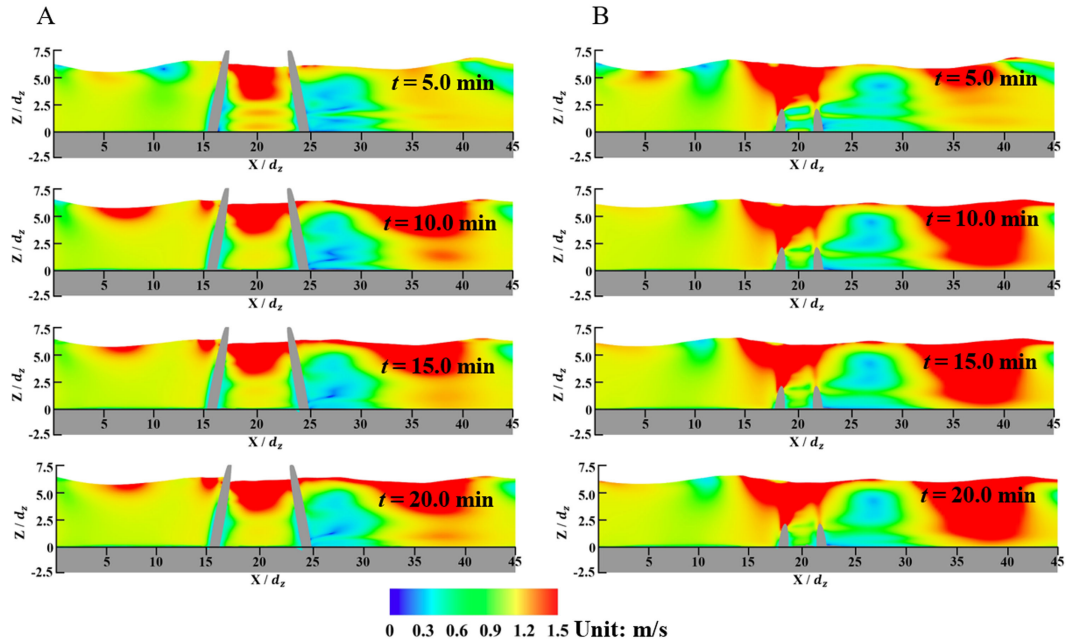

FIGURE 7
Velocity contours of the water flows on two typical *X*-*Z* planes for the original wind turbine. **(A)** In the plane of *Y* = 11.75 dz; **(B)** In the plane of *Y* = 14.50 dz.

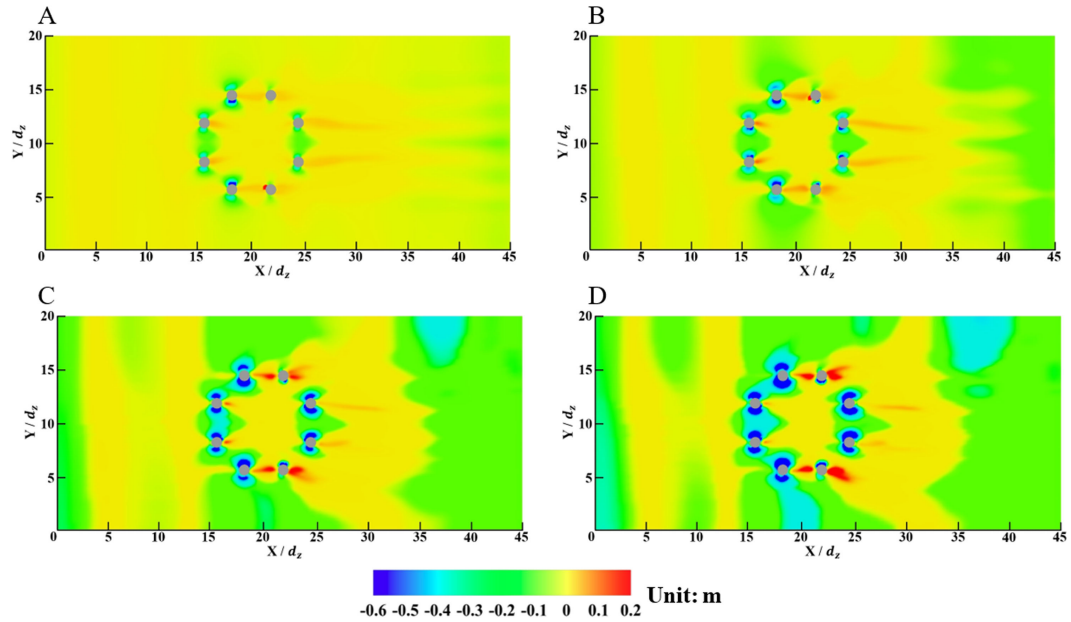

FIGURE 8
Depth contours from the reference plane near the piles for the original wind turbine (Z = 0). **(A)** t = 5.0 min; **(B)** t = 10.0 min; **(C)** t = 20.0 min; **(D)** t = 30.0 min.

of the distance between the tube ends and seabed on the velocity distribution of the water flow near the piles are minor. As the chamber tubes are close to the seabed (d_h = 1.25 dz), an enhancement of the large-velocity area in the rear of the tubes can be observed, which is caused by an increase in the water flow rate passing the tube ends because of the blockage of the added structures near the piles. In general, the prediction results show that the installation of the tube array has little influence on the flow field near the piles, indicating that the relative scale of the tube array is small compared to the original piles, which are the primary critical factors affecting the water flow field. The velocity contours of the water flow in the rear of the tube array in an X-Z plane (Y = 10.0 dz) for various values of d_h are depicted in Figure 11. The tube array has significant sheltered effects on the near field in their rear area with a reduction of the water flow velocity. The influence of sheltered effects on scouring depth was also found in previous studies (Amini et al., 2012; Ataie-Ashtiani and Beheshti, 2006). In general, in the X-Z plane, the installation of the OWC system also has limited influence on the water flow field in the rear of the tube array.

The velocity contours of the water flow near the piles in two typical X-Z planes at t = 30.0 min for various values of d_h are depicted in Figure 12. The flow fields near the piles for the wind-wave coupled device are similar to those for the original wind turbine in Figure 7. In addition, because of the blockage effects of the tube array, as the distance between the tube ends and seabed is relatively small, the velocities between the piles I and IV are enhanced, which might influence the sediment scouring and deposition near the piles. On the other hand, the sheltered effects

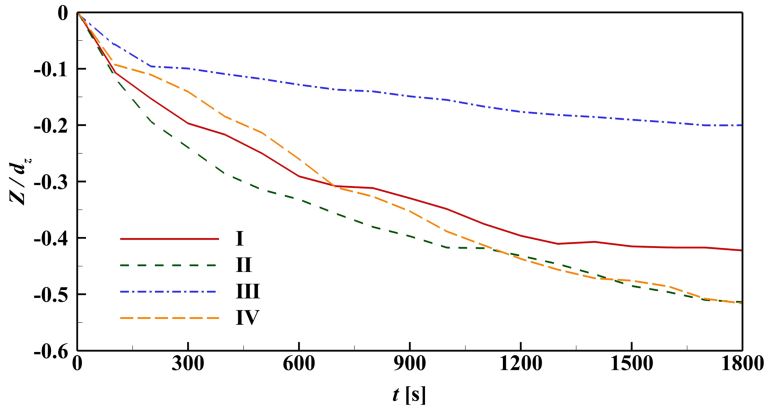

FIGURE 9
Depth variations at typical points near the piles for the original wind turbine.

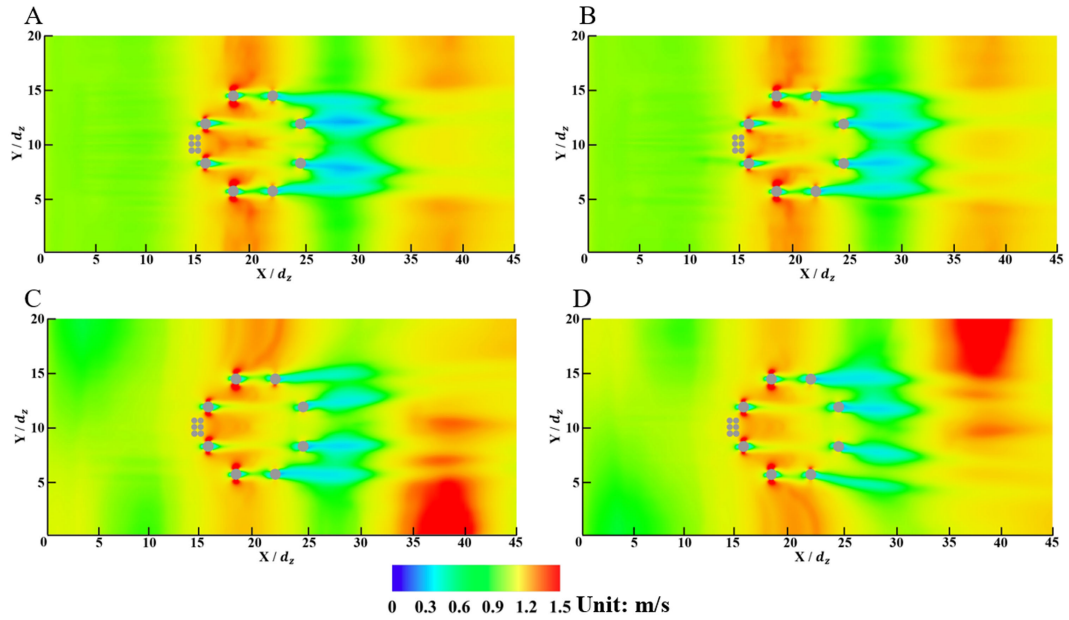

FIGURE 10
Velocity contours of the water flow on an *X*-*Y* plane for the wind-wave coupled device (*Z* = 0). **(A)** d_h = 1.25 dz; **(B)** d_h = 2.50 dz; **(C)** d_h = 3.75 dz; **(D)** d_h = 5.00 dz.

of Pile II on Pile III are still evident, resulting in an area with relatively small velocities. The tube array has no significant influence on the flow field distribution in this area.

The depth variations near the piles for the wind-wave coupled device at t = 30.0 min for various values of d_h are depicted in Figure 13. Compared to the depth variations for the original wind turbine in Figure 8, the differences of the sediment scouring and depositions near the piles are minor. The positions of the maximum scouring points near the piles have few differences. For instance, the differences in the positions near piles I and II for d_h = 1.25 dz and d_h = 2.50 dz are both less than 1% of the pile diameter, which can be ignored considering possible errors in the numerical simulations. Therefore, even for the wind-wave coupled device, the piles still play a critical role in the sediment movement nearby. In addition, for d_h = 1.25 dz and d_h = 2.50 dz, the scouring area surrounded by the piles becomes larger because of the velocity enhancement of the water flow caused by the tube array. The scouring depths are limited with the values less than 0.1 dz. As d_h > 2.50 dz, the scouring areas and depths are approximately the same as those for the original wind turbine.

The depth variations of the maximum scouring points near different piles during the simulation period for the coupled wind-wave device are depicted in Figure 14. In general, the existence of the tube array can accelerate the development of the scouring depth. For piles I to III, the maximum scouring depths are close to those for the original wind turbine. On the other hand, for the Pile IV and d_h = 5.00 dz, the OWC tubes have little influence on the maximum scouring depth. As the d_h value decreases, the maximum scouring depth shows a decreasing varying trend, and the scouring depth

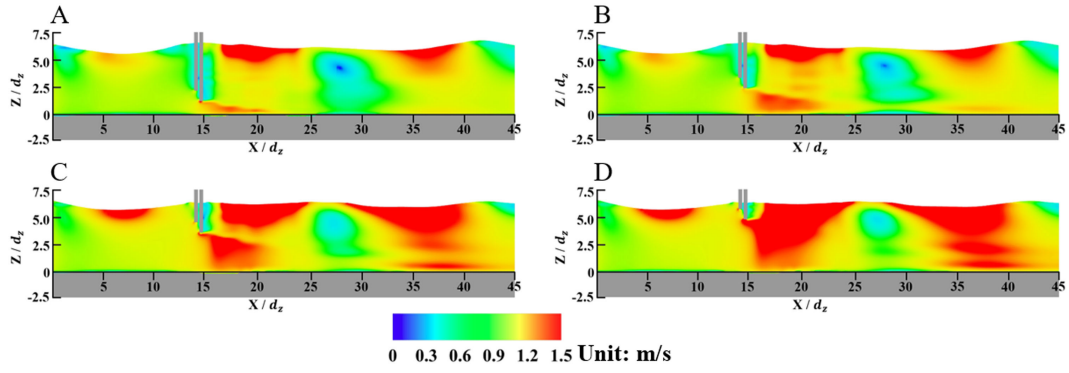

FIGURE 11
Velocity contours of the water flow in an *X*-*Z* plane for the wind-wave coupled device (*Y* = 10.0 dz). **(A)** d_h = 1.25 dz; **(B)** d_h = 2.50 dz; **(C)** d_h = 3.75 dz; **(D)** d_h = 5.00 dz.

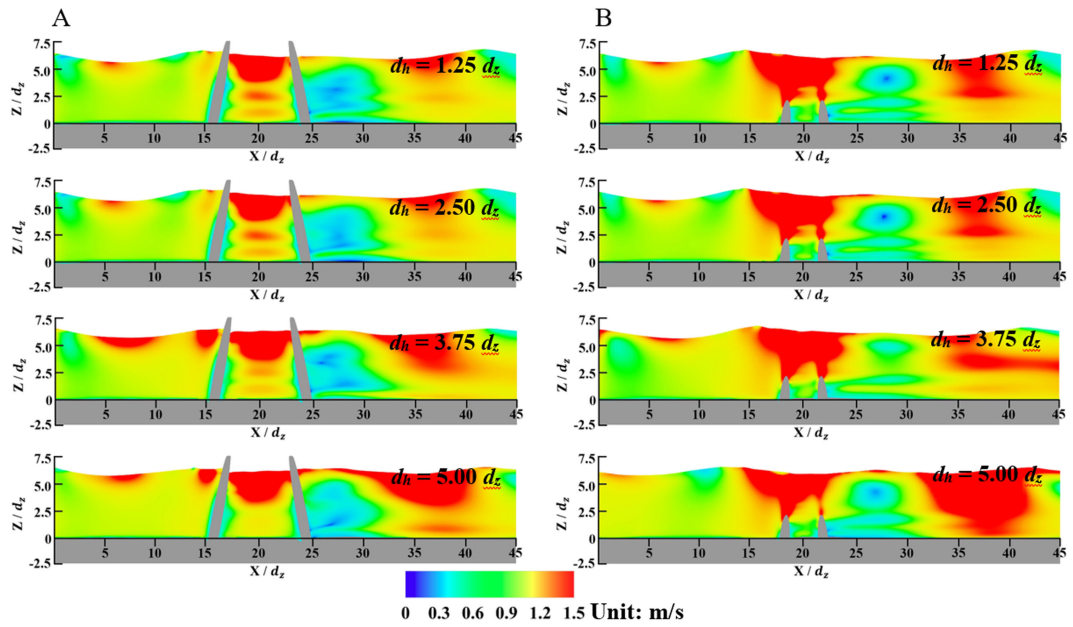

FIGURE 12
Velocity contours of the water flows on two typical *X*-*Z* planes for the wind-wave coupled device. **(A)** In the plane of *Y* = 11.75 dz; **(B)** In the plane of *Y* = 14.50 dz.

reduces 22.8% at t = 30.0 min compared to the case without any tubes. As mentioned, the scouring area surrounded by the piles increases, and the water flow can carry more sediment. When the water flow arrives at Pile IV, the velocity reduces because of the blockage of the pile, resulting in more sediment settlements.

The maximum scouring depths at the relative points near different piles for various values of d_h at t = 30.0 min are compared in Figure 15, where Z_{max} represents the maximum scouring depth near different piles. In general, installing the OWC system makes a minor contribution to the maximum

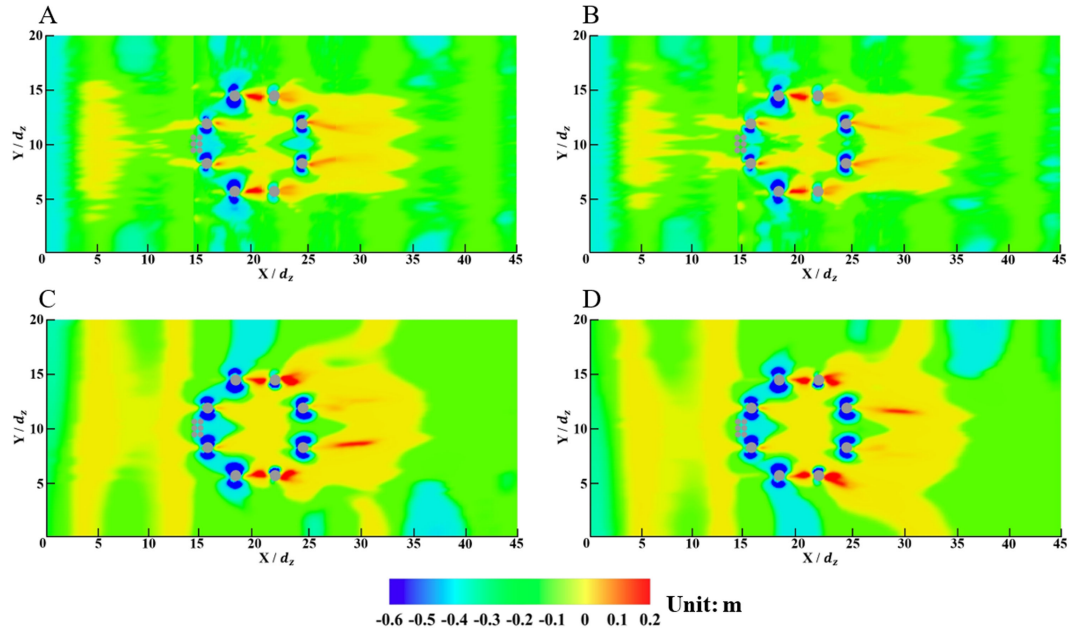

FIGURE 13
Depth contours from the reference plane near the piles for the wind-wave coupled device (*Z* = 0). **(A)** d_h = 1.25 dz; **(B)** d_h = 2.50 dz; **(C)** d_h = 3.75 dz; **(D)** d_h = 5.00 dz.

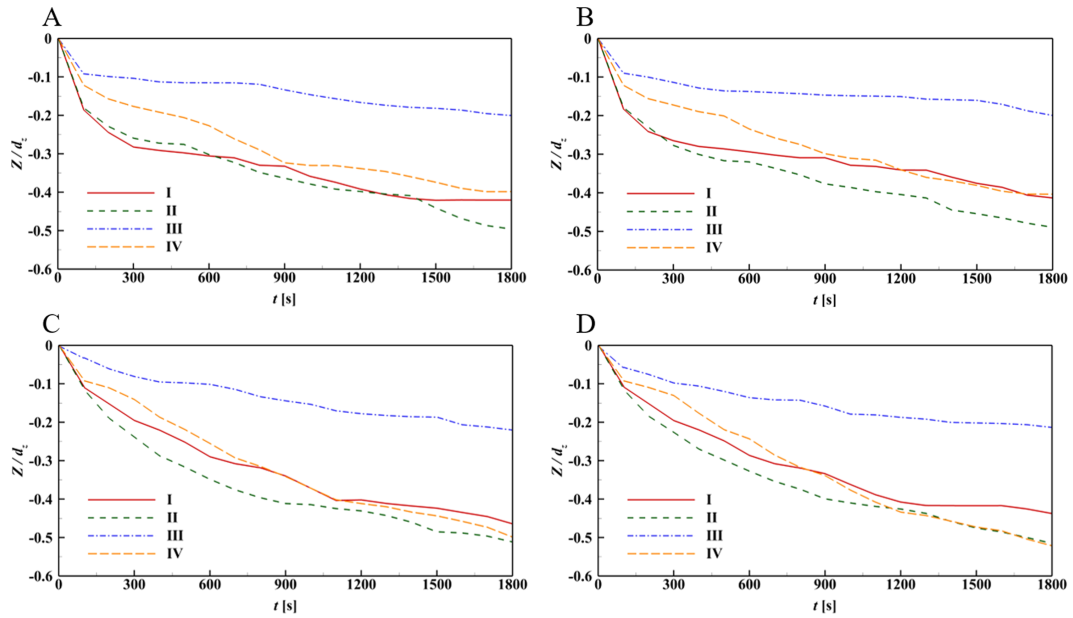

FIGURE 14
Depth variations at the maximum scouring points near the piles for the wind-wave coupled device. **(A)** d_h = 1.25 dz; **(B)** d_h = 2.50 dz; **(C)** d_h = 3.75 dz; **(D)** d_h = 5.00 dz.

scouring depths near different piles. On the contrary, as the tube end is close to the seabed, the existence of the tube array can significantly reduce the scouring depths near the piles, which is beneficial to the stability and reliability of the piles. No matter whether the OWC system is installed on the foundation of the offshore wind turbine, the sediment scouring depths near piles I&II and VII&VIII are relatively larger, and the protections should be conducted using various methods on the seabed near these piles.

5 Conclusions

A numerical model on the sediment scouring and deposition prediction near the piles for the fixed offshore wind turbine and an integrated OWC wave energy converter was established based on a commercial CFD platform, Flow 3D®, which was validated using experimental laboratory test data on a typical scouring problem. The sediment scouring and deposition near the foundation of an original wind turbine and a wind-wave coupled device under the

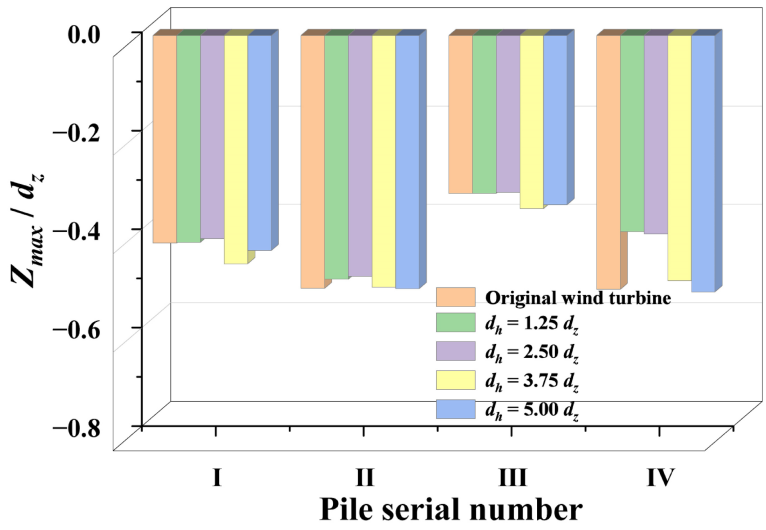

FIGURE 15
Maximum scouring depths near different piles for various d_h values.

joint actions of incident waves and currents for various tube end lengths are studied numerically.

Under the combined effect of waves and currents, the scouring phenomenon mainly occurs on both sides of the piles, while the deposition phenomenon takes place at the rear of the piles. Due to the relatively small distance between the piles in the direction of incident waves and currents, the blockage effect is significant, which leads to a reduction in scouring depth. When the piles are arranged in a staggered pattern, the blockage effect is reduced, and the flow field becomes more turbulent as it flows through the pipes, resulting in an increase in scouring depth.

The distance between the tube ends and the seabed has a notable impact on the scouring. When the distance is less than 2.5 times the pile diameter, the scouring area near the foundation is enlarged, and the development of the scouring is accelerated. However, the overall distribution of scour and deposition around each pile remains largely unaffected, and there is no significant increase in the maximum scouring depth near the piles. Additionally, although the OWC tubes increase the flow velocity around the seabed, the extent of this increase and the affected area are relatively small. The tubes also create a noticeable shielding effect behind them, which significantly reduces the scouring depth near the piles farther away. The closer the bottom of the tubes is to the seabed, the more pronounced the shielding effect becomes. This suggests that in engineering applications of the coupled wind and wave device, concerns about the bottom of the OWC device being too close to the seabed and causing increased foundation scour are unfounded.

Overall, the OWC tube arrays, or other configurations integrated with the wind turbine, have minimal influence on the scouring depth of the near piles and might cause a reduction in the maximum scouring depth near the piles at the far end, which is beneficial to the stability and reliability of the pile foundation of the coupled device. In the future, additional factors, such as the effects of different wind turbine foundations, marine environmental conditions, seabed geological conditions, and device scales on the scouring, will be considered to provide more comprehensive investigations of the device.

Data availability statement

The original contributions presented in the study are included in the article/supplementary material. Further inquiries can be directed to the corresponding author.

Author contributions

XC: Conceptualization, Investigation, Methodology, Writing – original draft. XY: Data curation, Investigation, Resources, Writing – review & editing. XD: Funding acquisition, Investigation, Visualization, Writing – review & editing. CX: Investigation, Methodology, Software, Writing – original draft. ZL: Conceptualization, Funding acquisition, Investigation, Supervision, Writing – review & editing. LW: Data curation, Software, Validation, Writing – review & editing.

Funding

The author(s) declare that financial support was received for the research and/or publication of this article. This work was supported by the Shandong Provincial Natural Science Foundation (Grant No. ZR2023QE110), National Natural Science Foundation of China (Grant Nos. 52301350 and 52471308) and the Project of Key Technology Research and Application of Fujian Coastal Wind and Wave Combined System (Grant No. 20240063).

Conflict of interest

Authors XC and XY were employed by Huadian Fujian Wind Power Co., Ltd.

The remaining authors declare that the research was conducted in the absence of any commercial or financial relationships that could be construed as a potential conflict of interest.

Generative AI statement

The author(s) declare that no Generative AI was used in the creation of this manuscript.

Publisher's note

References

Amini, A., Melville, B. W., Ali, T. M., and Ghazali, A. H. (2012). Clear-water local scour around pile groups in shallow-water flow. *J. Hydraul. Eng.* 138, 177–185. doi: 10.1061/(asce)hy.1943-7900.0000488

Analytis, G. T. (2003). Implementation of the renormalization group (RNG) k-ε turbulence model in GOTHIC/6.1b: Solution methods and assessment. *Ann. Nucl. Energy* 30, 349–387. doi: 10.1016/S0306-4549(02)00061-0

Ataie-Ashtiani, B., and Beheshti, A. A. (2006). Experimental investigation of clear-water local scour at pile groups. *J. Hydraul. Eng.* 132, 1100–1104. doi: 10.1061/(asce)0733-9429(2006)132:10(1100

Bordbar, A., Sharifi, S., and Hemida, H. (2021). Investigation of the flow behaviour and local scour around single square-shaped cylinders at different positions in live-bed. *Ocean Eng.* 238, 109772. doi: 10.1016/j.oceaneng.2021.109772

De Azevedo, H. D. M., Araújo, A. M., and Bouchonneau, N. (2016). A review of wind turbine bearing condition monitoring: State of the art and challenges. *Renew. Sustain. Energy Rev.* 56, 368–379. doi: 10.1016/j.rser.2015.11.032

Dixen, M., Sumer, B. M., and Fredsøe, J. (2013). Numerical and experimental investigation of flow and scour around a half-buried sphere. *Coast. Eng.* 73, 84–105. doi: 10.1016/j.coastaleng.2012.10.006

Fernandez Luque, R., and Van Beek, R. (1976). Erosion and transport of bed-load sediment. *J. Hydraul. Res. Rech. Hydraul.* 14, 127–144. doi: 10.1080/00221687609499677

Flow Science. (2016). *FLOW-3D® Version 11.2 Users Manual*. Santa Fe, NM: Flow Science, Inc. Available online at: https://www.flow3d.com.

Hu, R., Wang, X., Liu, H., and Lu, Y. (2021). Experimental study of local scour around tripod foundation in combined collinear waves-current conditions. *J. Mar. Sci. Eng.* 9 (12), 1373. doi: 10.3390/jmse9121373

Kim, H. S., Nabi, M., Kimura, I., and Shimizu, Y. (2014). Numerical investigation of local scour at two adjacent cylinders. *Adv. Water Resour.* 70, 131–147. doi: 10.1016/j.advwatres.2014.04.018

Li, J., Guo, Y., Lian, J., and Wang, H. (2022). Scour effects on the bearing capacity of multi-bucket jacket foundation for offshore wind turbines. *Ocean Eng.* 259, 111848. doi: 10.1016/j.oceaneng.2022.111848

Liang, F., Wang, C., Huang, M., and Wang, Y. (2017). Experimental observations and evaluations of formulae for local scour at pile groups in steady currents. *Mar. Georesources Geotechnol.* 35, 245–255. doi: 10.1080/1064119X.2016.1147510

Liu, D., Diplas, P., Fairbanks, J. D., and Hodges, C. C. (2008). An experimental study of flow through rigid vegetation. *J. Geophys. Res. Earth Surf.* 113, 1–16. doi: 10.1029/2008JF001042

Liu, M. M., Wang, H. C., Tang, G. Q., Shao, F. F., and Jin, X. (2022). Investigation of local scour around two vertical piles by using numerical method. *Ocean Eng.* 244, 110405. doi: 10.1016/j.oceaneng.2021.110405

Mastbergen, D. R., and Van Den Berg, J. H. (2003). Breaching in fine sands and the generation of sustained turbidity currents in submarine canyons. *Sedimentology* 50, 625–637. doi: 10.1046/j.1365-3091.2003.00554.x

Menéndez-Vicente, C., López-Querol, S., Bhattacharya, S., and Simons, R. (2023). Numerical study on the effects of scour on monopile foundations for Offshore Wind Turbines: The case of Robin Rigg wind farm. *Soil Dyn. Earthq. Eng.* 167, 107803. doi: 10.1016/j.soildyn.2023.107803

Okhravi, S., Gohari, S., Alemi, M., and Maia, R. (2023). Numerical modeling of local scour of non-uniform graded sediment for two arrangements of pile groups. *Int. J. Sediment Res.* 38, 597–614. doi: 10.1016/j.ijsrc.2023.04.002

Olsen, N. R. B., and Kjellesvig, H. M. (1998). Three-dimensional numerical flow modeling for estimation of maximum local scour depth. *J. Hydraul. Res.* 36, 579–590. doi: 10.1080/00221689809498610

Qi, W. G., and Gao, F. P. (2014). Physical modeling of local scour development around a large-diameter monopile in combined waves and current. *Coast. Eng.* 83, 72–81. doi: 10.1016/j.coastaleng.2013.10.007

Rehman, S., Alhems, L. M., Alam, M. M., Wang, L., and Toor, Z. (2023). A review of energy extraction from wind and ocean: Technologies, merits, efficiencies, and cost. *Ocean Eng.* 267, 113192. doi: 10.1016/j.oceaneng.2022.113192

Roulund, A., Sumer, B. M., Fredsøe, J., and Michelsen, J. (2005). Numerical and experimental investigation of flow and scour around a circular pile. *J. Fluid Mech.* 534, 351–401. doi: 10.1017/S0022112005004507

Steven, F., Thomas, A., and Paul, E. (1990). A taxonomy for conjugate gradient methods. *SIAM J. Numer. Anal.* 27, 1542–1568. doi: 10.1137/0727091

Wan, L., Moan, T., Gao, Z., and Shi, W. (2024). A review on the technical development of combined wind and wave energy conversion systems. *Energy* 294, 130885. doi: 10.1016/j.energy.2024.130885

Wang, W., Yang, S., Gao, C., and Huang, W. (2020). Influence of turbulence schmidt number on exit temperature distribution of an annular gas turbine combustor using flamelet generated manifold. *J. Therm. Sci.* 29, 58–68. doi: 10.1007/s11630-019-1248-8

Welzel, M., Schendel, A., Hildebrandt, A., and Schlurmann, T. (2019). Scour development around a jacket structure in combined waves and current conditions compared to monopile foundations. *Coast. Eng.* 152, 103515. doi: 10.1016/j.coastaleng.2019.103515

Yang, X., Liu, N., Zhang, P., Guo, Z., Ma, C., Hu, P., et al. (2019). The current state of marine renewable energy policy in China. *Mar. Policy* 100, 334–341. doi: 10.1016/j.marpol.2018.11.038

Yeh, P. H., Chang, K. A., Henriksen, J., Edge, B., Chang, P., Silver, A., et al. (2009). Large-scale laboratory experiment on erosion of sand beds by moving circular vertical jets. *Ocean Eng.* 36, 248–255. doi: 10.1016/j.oceaneng.2008.11.006

Yu, T., Lian, J., Shi, Z., and Wang, H. (2016). Experimental investigation of current-induced local scour around composite bucket foundation in silty sand. *Ocean Eng.* 117, 311–320. doi: 10.1016/j.oceaneng.2016.03.045

Yu, T., Zhang, Y., Zhang, S., Shi, Z., Chen, X., Xu, Y., et al. (2019). Experimental study on scour around a composite bucket foundation due to waves and current. *Ocean Eng.* 189, 106302. doi: 10.1016/j.oceaneng.2019.106302

Zhang, F., Chen, X., Feng, T., Wang, Y., Liu, X., and Liu, X. L. (2022). Experimental study of grouting protection against local scouring of monopile foundations for offshore wind turbines. *Ocean Eng.* 258, 111798. doi: 10.1016/j.oceaneng.2022.111798

Zhang, F., Chen, X., Feng, T., and Zhang, Y. (2023). Experimental investigation of the horizontal bearing capacity of offshore wind-turbine monopiles with grouting protection against scouring. *Ocean Eng.* 280, 114848. doi: 10.1016/j.oceaneng.2023.114848

Zhang, Q., Zhou, X. L., and Wang, J. H. (2017). Numerical investigation of local scour around three adjacent piles with different arrangements under current. *Ocean Eng.* 142, 625–638. doi: 10.1016/j.oceaneng.2017.07.045

Zhao, M., Cheng, L., and Zang, Z. (2010). Experimental and numerical investigation of local scour around a submerged vertical circular cylinder in steady currents. *Coast. Eng.* 57, 709–721. doi: 10.1016/j.coastaleng.2010.03.002

Zheng, Y., Zhang, J., Xie, W., Zhu, L., Guo, T., and Pan, J. (2024). Numerical study of local scour around a cubic artificial reef in steady current. *Ocean Eng.* 311, 118851. doi: 10.1016/j.oceaneng.2024.118851

Glossary

A_x	Area fraction of the fluid in x direction	V_F	Volume fraction of the flow section
S_c	Reciprocal of the turbulent Schmidt number	g	Gravitational acceleration
A_y	Area fraction of the fluid in y direction	w	Velocity components in the z direction
T	Wave period	G	Components of the gravitational acceleration
A_z	Area fraction of the fluid in z direction	α	Entrainment parameter
u	Velocity components in the x direction	h_s	Height of the shared chamber
$C_{s,I}$	Mass concentration of the suspended sediment	β	Bed load coefficient
u_f	Dynamic viscosity of water	h_t	Height of the short tubes
d_c	Tube diameter	Δ	Difference of the short and long tubes
u_{lift}	Entrainment lift velocity of the sediment	H	Wave height
d_h	Distance between the seabed and the longest tube	θ_{cr}	Threshold Shields number
$u_{settling}$	Settling velocity of the sediment	H_c	Height of the reinforced concrete cap
d_i	Sediment median diameter	θ_i	Local Shields number
$u_{s,I}$	Velocity of the suspended load	N_s	Outward pointing normal to the packed bed interface
d_z	Pile diameter	ρ	Water density
v	Velocity components in the y direction	p	Pressure of water
D	Sediment diffusion coefficient	ρ_i	Sediment density
ν_f	Kinematic viscosity of water	$q_{b,I}$	Bed load discharge
D_c	Diameter of the reinforced concrete cap	τ	Local bed shear stress
ν_ρ	Coefficient of momentum diffusion	R_{DIF}	Turbulent diffusion term
f	Components of the viscous acceleration	Φ_i	Coefficient of the bed load discharge.